


Article

# Effect of Sr-Doping on the Photocatalytic Performance of $\text{LaNiO}_{3-\sigma}$

Yuhao Zhang <sup>†</sup>, Liang Guo <sup>\*,†</sup>, Qunang Xu, Qingmao Zhang, Jiaming Li  and Qiongiong Ma

Guangdong Provincial Key Laboratory of Nanophotonic Functional Materials and Devices, School of Information and Optoelectronic Science and Engineering, South China Normal University, Guangzhou 510006, China

\* Correspondence: guoliangchn@163.com

<sup>†</sup> These authors contributed equally to this work.

**Abstract:** In this study, to investigate how oxygen vacancy impacts the photocatalytic performance of  $\text{LaNiO}_3$ , undoped and Sr-doped  $\text{LaNiO}_{3-\sigma}$  nanoparticles are successfully prepared by the sol-gel method. The X-ray diffractometer (XRD) results show both two samples belong to the R-3c space group of the rhombohedral system. According to the conservation of valence and the X-ray photoelectron spectroscopy (XPS) results, it is demonstrated that Sr-doping can introduce more oxygen vacancy into  $\text{LaNiO}_{3-\sigma}$ . According to photocatalytic experiments of the degradation of methyl orange (MO) solution,  $\text{La}_{0.875}\text{Sr}_{0.125}\text{NiO}_{3-\sigma}$  shows higher photocatalytic performance than undoped  $\text{LaNiO}_{3-\sigma}$ . First-principle calculation results show that the introduction of oxygen vacancy and Sr-doping can lead to the narrowing of the band gap width of  $\text{LaNiO}_3$ .

**Keywords:** perovskite; photocatalyst; oxygen vacancy; first-principle



**Citation:** Zhang, Y.; Guo, L.; Xu, Q.; Zhang, Q.; Li, J.; Ma, Q. Effect of Sr-Doping on the Photocatalytic Performance of  $\text{LaNiO}_{3-\sigma}$ . *Catalysts* **2022**, *12*, 1434. <https://doi.org/10.3390/catal12111434>

Academic Editor: Hamidreza Arandiyani

Received: 12 October 2022

Accepted: 10 November 2022

Published: 15 November 2022

**Publisher's Note:** MDPI stays neutral with regard to jurisdictional claims in published maps and institutional affiliations.



**Copyright:** © 2022 by the authors. Licensee MDPI, Basel, Switzerland. This article is an open access article distributed under the terms and conditions of the Creative Commons Attribution (CC BY) license (<https://creativecommons.org/licenses/by/4.0/>).

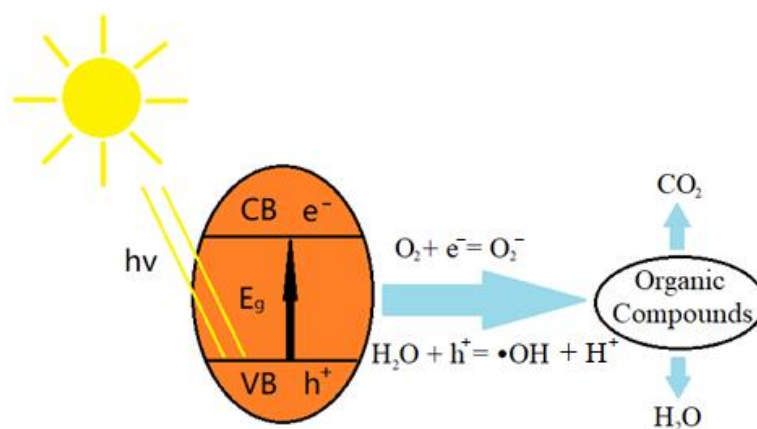
## 1. Introduction

Since Fujishima A. [1] observed the decomposition of water on the  $\text{TiO}_2$  electrode, the semiconductor photocatalysts have received more attention. In recent years, more and more semiconductors have been used as photocatalysts, which have shown an excellent photocatalytic effect. Novel photocatalytic technology is gradually applied to energy shortage and environmental pollution problems [2]. At present, perovskite semiconductors have been used in the field of photocatalytic energy conversion, which has good metal ground state, electrochemical performance, high discharge capacity, electrical conductivity, and other physical properties. Perovskite oxides have the general formula  $\text{ABO}_3$ , where A (usually in the +3 state) is likely to be rare earth or alkaline earth metal cations, and B (usually in the +3 state) is likely to be transition metal cations. In addition, perovskite oxides have been utilized in  $\text{CO}_2$  reduction [3–7],  $\text{H}_2$  production of water decomposition [8–12], solid oxide fuel cells [13–16], and photocatalytic degradation of organic pollutants [17,18]. Many internal factors impact photocatalysts, such as band structure, quantum efficiency, specific surface area, and lattice defects. Many methods are used to improve perovskite oxide photocatalysts, such as doping [4,13,19], noble metal modification [20,21], semiconductor recombination [22,23], and so on.

Perovskites with well-defined crystal structures exhibit specific chemical and physical properties, which provide a favorable substrate for chemical substitutions at the A and B sites.  $\text{LaNiO}_3$  belongs to such  $\text{ABO}_3$  perovskite class and possesses a rhombohedral structure with space group R-3c [24].  $\text{LaNiO}_3$  has attained much attention as a photocatalyst due to its high photocatalytic performance, chemical and thermal stability, and economic and ecofriendly nature.  $\text{LaNiO}_3$  perovskite oxide is widely utilized in various applications with promising optical, electrical, and magnetic properties [25]. The low-temperature nanometer preparation method of chemically assisted electrodeposition (CAED) has proved the application of  $\text{LaNiO}_3$  electrocatalyst as cathode material of solid oxide fuel cell (SOFC) for the first time. Compared with the sintering method or self-assembly method, CAED

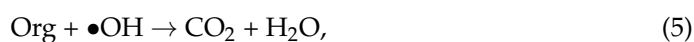
is a better method for producing LaNiO<sub>3</sub>/GDC composite cathode of SOFCs, which can improve the material properties [26]. Reactive oxygen species (O<sup>-</sup> or O<sub>2</sub><sup>2-</sup>) exist not only on the surface of perovskite oxides but also on a large number of other oxides. In addition, the synergistic effect of transition metal ions with high oxidation states and randomly dispersed oxygen vacancy are crucial factors determining the photocatalytic performance of perovskite oxides [27]. Oxygen vacancy content  $\sigma$  of (Sr<sub>0.776</sub>La<sub>0.224</sub>)<sub>4</sub>Fe<sub>3</sub>O<sub>10- $\delta$</sub>  (SLF4310, number of perovskite layers  $n = 3$ ) was studied by iodine titration and thermogravimetric analysis. The equilibrium constant of the reduction reaction of SLF4310 was estimated according to the temperature dependence of oxygen vacancy content  $\delta$  [28]. The electronic structure and optical properties of perfect and imperfect LaNiO<sub>3</sub> are also presented in ab initio methods [29,30]. A series of cellular perovskite oxide La<sub>1-x</sub>Sr<sub>x</sub>NiO<sub>3- $\delta$</sub>  composites were successfully prepared by a simple and extensible sol-gel method combining annealing and Sr-doping with different content [31]. It has been verified that oxygen vacancy can enhance the visible response and improve the photocatalytic performance for a series of materials, such as WO<sub>3</sub> [32], TiO<sub>2</sub> [33,34], C<sub>3</sub>N<sub>4</sub> [35–37], LaFeO<sub>3</sub> [38,39].

Figure 1 shows the proposed photocatalytic mechanism in the photocatalytic process. The surface of the photocatalyst is exposed to enough light intensity and generates electron-hole pairs. When the photocatalyst contacts the pollutant receptor, the holes (h<sup>+</sup>) on the surface of the photocatalyst would undergo oxidation-reduction reactions with organic pollutants. Moreover, strong oxidizing substances such as holes and hydroxyls produced by photocatalysts can degrade organic pollutants into CO<sub>2</sub> and H<sub>2</sub>O. On the one hand, the content of holes is high, which plays the main role in oxidative degradation. On the other hand, hydroxyl has strong oxidation, but its content is low, which plays an auxiliary role in oxidation.



**Figure 1.** The photocatalytic mechanism for photocatalysts under simulated solar irradiation.

The photocatalytic process can be expressed as the following reaction:



where e<sup>-</sup> is the electron, h<sup>+</sup> is the hole, •OH and Org are the hydroxyl and the organic compounds, respectively. Under simulated solar radiation, the excited electrons were captured by oxygen vacancy on the surface of undoped and Sr-doped LaNiO<sub>3- $\sigma$</sub>  and reacted with O<sub>2</sub> to produce O<sub>2</sub><sup>-</sup>. Moreover, O<sub>2</sub><sup>-</sup> will react with H<sup>+</sup> and e<sup>-</sup> to •OH, and the photogenerated holes (h<sup>+</sup>) from the valence band will react with H<sub>2</sub>O to produce •OH

radicals. Finally,  $h^+$  and  $\bullet OH$  react together with organic compounds to produce  $CO_2$  and  $H_2O$ . The photocatalytic process occurs when organic compounds are adsorbed on the surface of photocatalysts. Oxygen vacancy can act as an electron or hole capture center, which is beneficial to inhibit the coincidence of the photogenerated electron-hole pairs and, thus, improve the photocatalytic performance of the photocatalyst.

The defect-mediated synthesis of materials usually involves annealing in a reducing atmosphere or under a high vacuum at high temperatures (150 °C) [40,41]. These methods usually suffer from some drawbacks, such as requiring high energy consumption or complicated facilities. In a previous study, because of the metal transition element on the B site or the synthesis condition,  $LaNiO_3$  is a non-stoichiometric compound and might have oxygen vacancy in nature [42,43]. However, there are few reports about introducing more oxygen vacancy into  $LaNiO_3$ . Therefore, the challenge remains in finding a simple and convenient method to prepare  $LaNiO_3$  with more oxygen vacancy.

As for  $LaNiO_{3-\sigma}$  and  $SrNiO_{3-\sigma}$ , the lack of lattice oxygen has a great influence on the physical properties and material properties of perovskite oxides. Based on these two kinds of perovskite metal oxides, the La element is +3 state, and the Sr element is +2 state, so Ni belongs to the +3 state in  $LaNiO_{3-\sigma}$  and +4 state in  $SrNiO_{3-\sigma}$ . It is indicated that the valence state of the Ni element in perovskite oxide would vary with other changes as the A site element changes. Therefore, according to the nature of the transition metal element, Ni has three states, such as +2, +3, and +4, and then doping Sr element in A site of  $LaNiO_3$  might cause extreme instability of the valence state of Ni element, and thus introduce more oxygen vacancy.

The main work of this paper is to prepare undoped and Sr-doped  $LaNiO_{3-\sigma}$  by the sol-gel method and explore the effect of Sr-doping on the oxygen vacancy with the lower valence element doping at the A site. The  $LaNiO_{3-\sigma}$  and  $La_{1-x}Sr_xNiO_{3-\sigma}$  perovskite powder samples will be characterized by XRD, SEM, and XPS to study the crystal phase, microscopic appearance, and valence states of elements, respectively. In addition, the analysis results of the photocatalytic degradation experiment are detected by UV-Vis spectrophotometer to study the photocatalytic performance of  $LaNiO_{3-\sigma}$  and  $La_{1-x}Sr_xNiO_{3-\sigma}$ . As a pH indicator, methyl orange (Figure 2) has been widely utilized in laboratory and industrial production and can also be used for halogen content detection and biological staining. Therefore, methyl orange was used as the degradation pollutant in this study. First principle calculations are used to study how Sr-doping and the oxygen vacancy impact the band structure and density of states of  $LaNiO_{3-\sigma}$  and  $La_{1-x}Sr_xNiO_{3-\sigma}$ . In conclusion, according to the conservation of valence, a method of improving photocatalytic performance by introducing more oxygen vacancy is investigated.

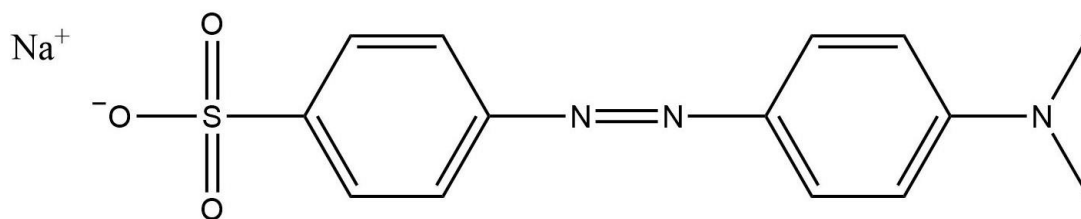


Figure 2. Chemical structure of methyl orange.

## 2. Results and Discussion

### 2.1. Morphology

#### 2.1.1. X-ray Diffractometer

The crystal phases of undoped and Sr-doped  $LaNiO_{3-\sigma}$  are characterized by an X-ray diffractometer (XRD). As shown in Figure 3a, it is observed that the crystal phases of both photocatalysts are related to JCPDS card No. 34-1028, which belongs to the R-3c space group of the rhombohedral system. The peaks located at 23.3°, 32.9°, 40.7°, 41.3°, 47.4°, 53.3°, 58.7°, and 68.9° can be readily indexed to (101), (110), (021), (003), (202), (211), (122), (220) planes of rhombohedral  $LaNiO_3$  (JCPDS card No. 34-1028). The 37.2° and 43.3° peaks

of NiO are too low, so the content of NiO is very small, which has little influence on the subsequent photocatalytic experiments.

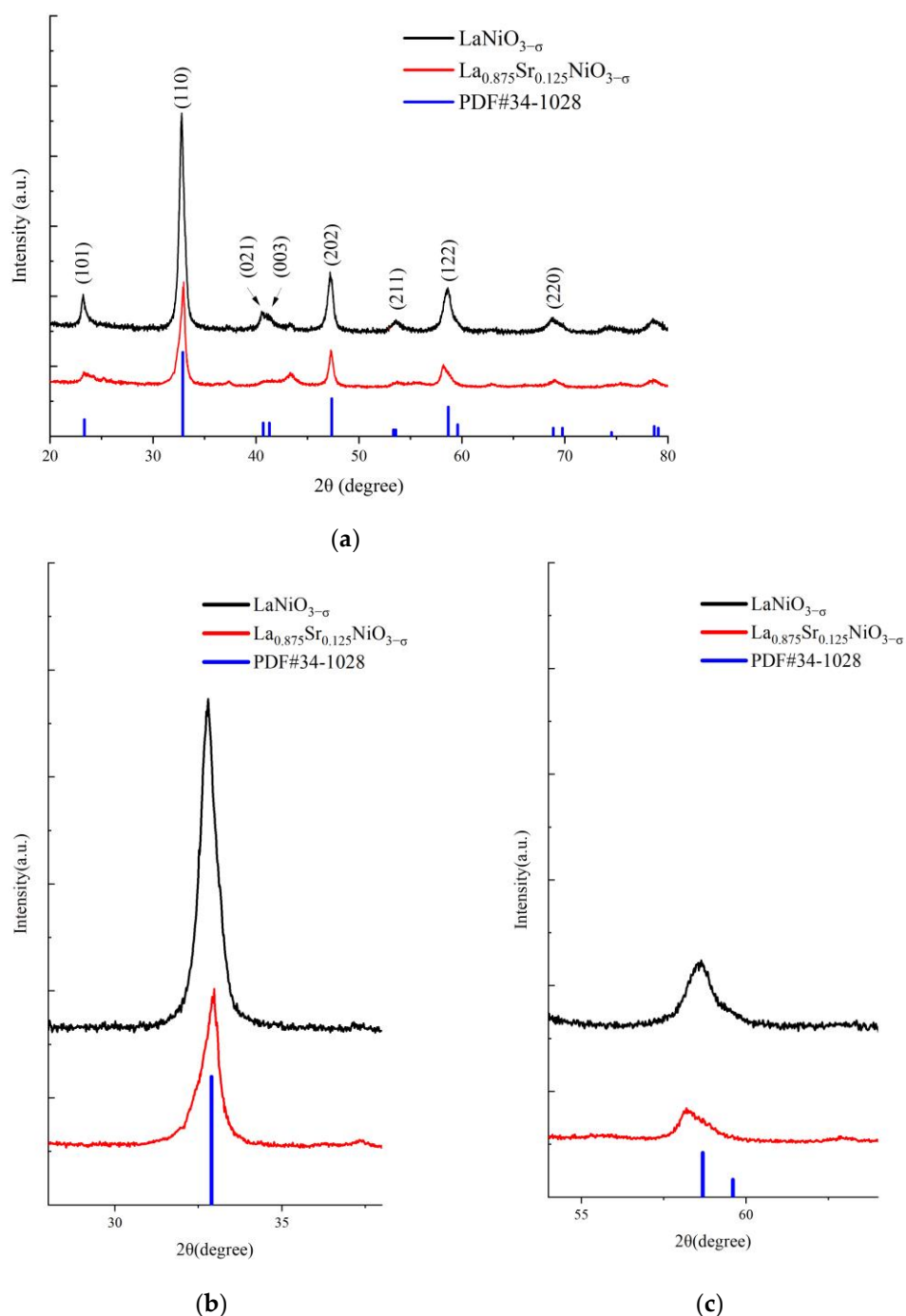


**Figure 3.** XRD spectrum of undoped and Sr-doped  $\text{LaNiO}_{3-\sigma}$ . (a) Full spectrum; (b) range 28°–38°; (c) range 54°–64°.

Sr-doping could cause changes in the lattice parameters due to different iron radii. As shown in Figure 3b, it is observed that the diffraction peak of Sr-doped  $\text{LaNiO}_{3-\sigma}$  at about 32.77° shifted to a higher angle than that of undoped  $\text{LaNiO}_{3-\sigma}$ , indicating that Sr-doping led to a decrease in the lattice parameters of  $\text{LaNiO}_{3-\sigma}$ .

However, as shown in Figure 3c, the diffraction peak of Sr-doped  $\text{LaNiO}_{3-\sigma}$  at about 58.57° shifted to a lower angle than that of undoped  $\text{LaNiO}_{3-\sigma}$ , indicating that Sr-doping also led to an increase in the lattice parameters of  $\text{LaNiO}_{3-\sigma}$ . It means Sr-doping will not

necessarily cause global changes in lattice parameters. Since the ionic radius of  $\text{Sr}^{2+}$  ion (0.113 nm) is larger than that of  $\text{La}^{3+}$  ion (0.106 nm), the Sr-doping in the substitutional sites will lead to an increase in some of the lattice parameters. In the meanwhile, Sr-doping would lead to more transitions of  $\text{Ni}^{3+}$  ion to  $\text{Ni}^{4+}$  ion, and the ion radius of  $\text{Ni}^{4+}$  (0.048 nm) is smaller than that of  $\text{Ni}^{3+}$  (0.062 nm), which will lead to a decrease in the other of the lattice parameters. It is indicated that the Sr element is successfully doped in the A site of  $\text{LaNiO}_{3-\sigma}$  with no crystal phase transition.

### 2.1.2. Scanning Electron Microscopy

The Scanning electron microscopy (SEM) results of undoped and Sr-doped  $\text{LaNiO}_{3-\sigma}$  are shown in Figure 4a,b, respectively, magnified by 50 k times. In addition, Figure 4c,d are the SEM images of undoped and Sr-doped  $\text{LaNiO}_{3-\sigma}$  magnified by 100 k times, respectively. It can be observed that the undoped and Sr-doped  $\text{LaNiO}_{3-\sigma}$  powder crystallized well under the predetermined experimental conditions, and the powder particles have formed agglomerates partially. The particle size distribution is in the range of 80–150 nm. Due to the small particle size and Van Der Waals force, the powder particles would interact with each other to form agglomerates.

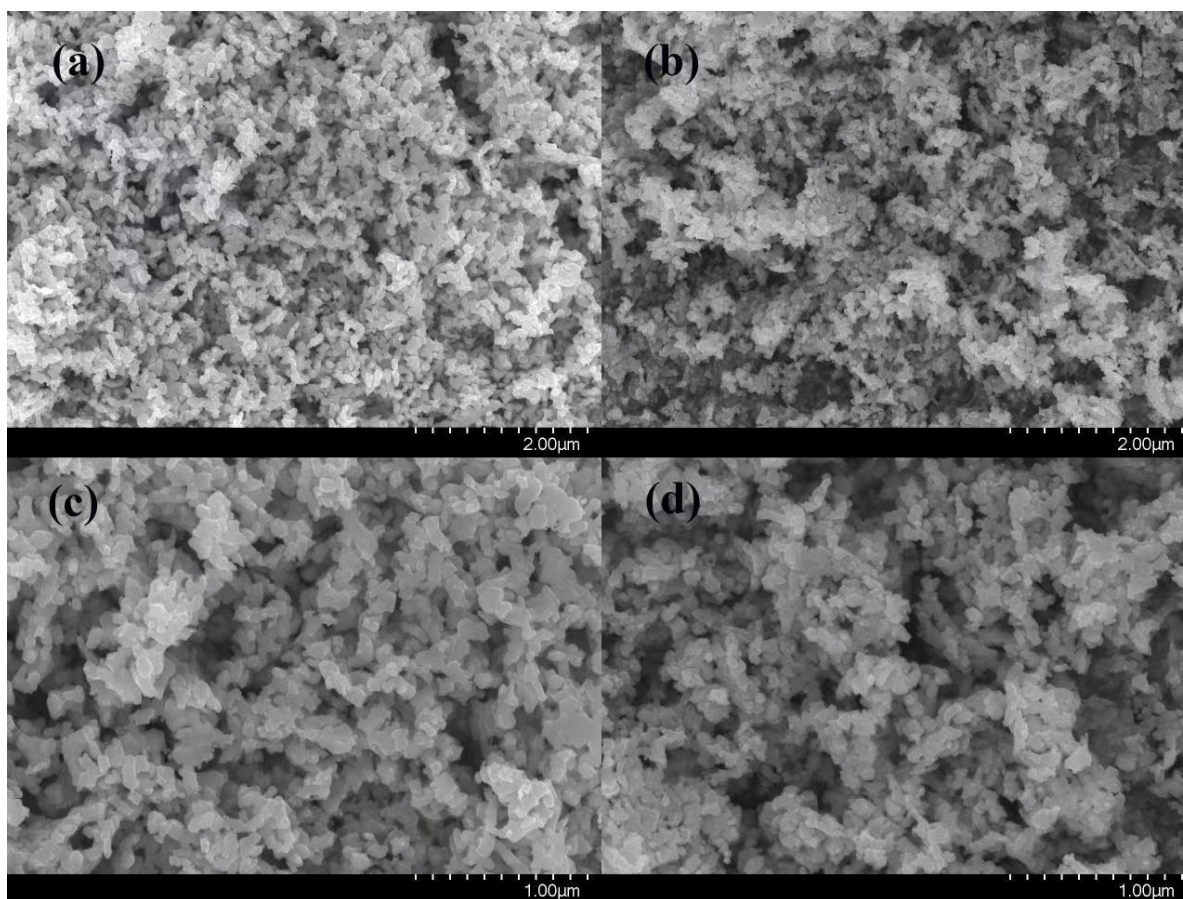


**Figure 4.** SEM image of 50 k and 100 k magnification times of (a,c) undoped  $\text{LaNiO}_{3-\sigma}$  and (b,d) Sr-doped  $\text{LaNiO}_{3-\sigma}$ .

### 2.2. X-ray Photoelectron Spectroscopy

The surface chemical states were studied by X-ray photoelectron spectroscopy (XPS), which is used to characterize the elemental composition through qualitative analysis and elemental valence analysis on the powder sample surface. As shown in Figure 5a, the XPS spectrum was scanned extensively in the range of 0–1000 eV. The full scan spectrum of Sr-doped  $\text{LaNiO}_{3-\sigma}$  has a more Sr-3d signal peak than that of undoped  $\text{LaNiO}_{3-\sigma}$ ,

in which all peaks belong to elements labeled as La, Sr, Ni, O, and C, and there are no additional peaks corresponding to impurities. The peaks in 600–800 eV attribute to the Auger effect peaks of Ni, including Ni-LM2, Ni-LM5, and Ni-LM8. The peak of 974 eV belongs to the Auger effect peak of O, which is attributed to O-LK1. As shown in Figure 5b, the emerged C-1s peaks at 284.8 eV and 289.5 eV are attributed to the carbon supporting film on the grid [41], which is used to calibrate other binding energy in the spectrum.

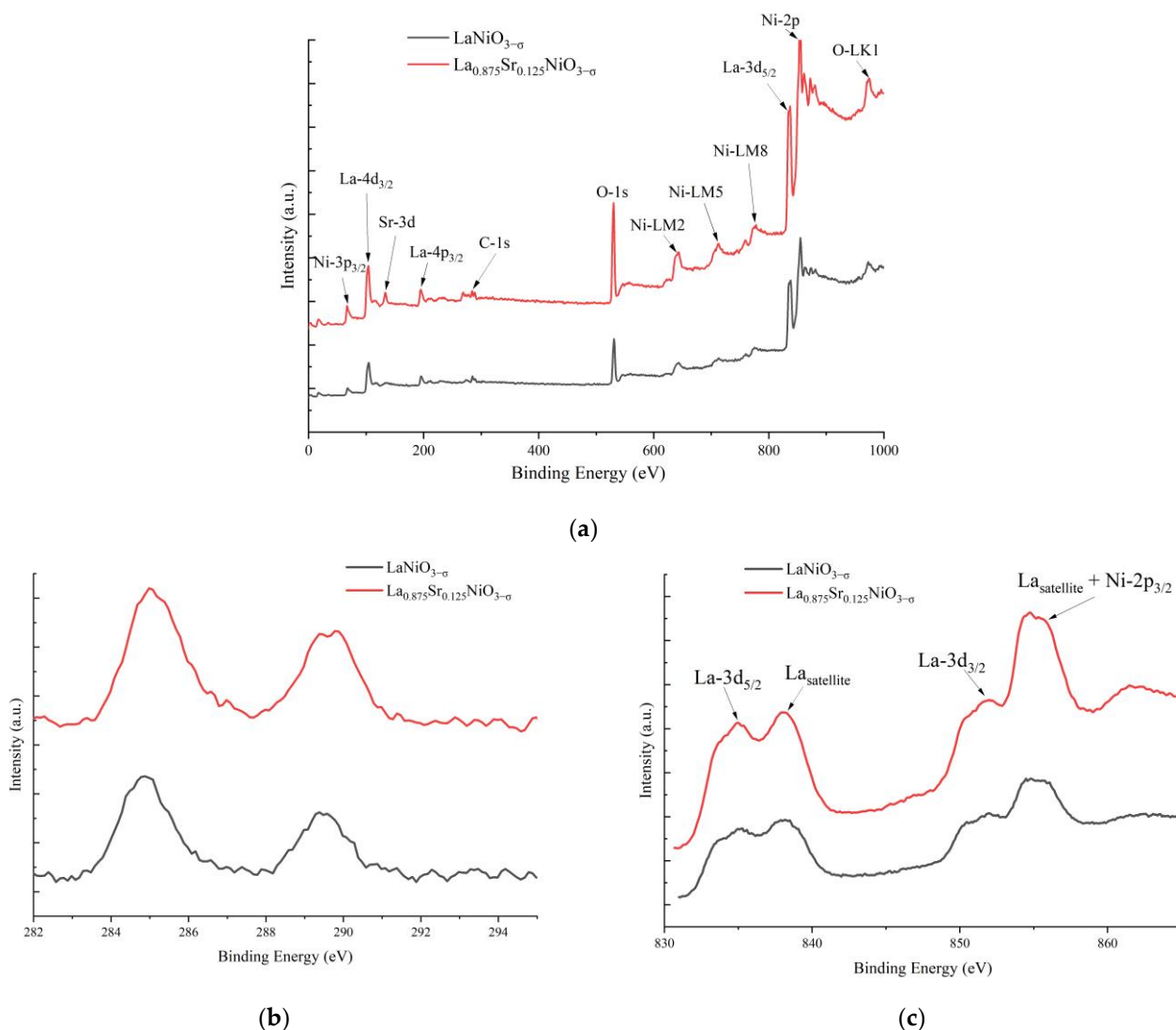


**Figure 5.** XPS spectrum of undoped and Sr-doped  $\text{LaNiO}_{3-\sigma}$ . (a) Full scan; (b) C-1s scan; (c) La-3d & Ni-2p scan.

The La-3d and Ni-2p core-level spectrum is shown in Figure 5c; both undoped and Sr-doped  $\text{LaNiO}_{3-\sigma}$  almost have the same signal peaks. On account of the coupling of spin-orbit splitting and multi-splitting, both La-3d and Ni-2p core-level spectra show very complicated multi-component structures. It is observed that La-3d<sub>5/2</sub> and La-3d<sub>3/2</sub> peaks both appear with the satellite peak, while the Ni-2p<sub>3/2</sub> peak is strongly overlapped with the La-3d<sub>3/2</sub> satellite peak [44]; therefore, it is too difficult to calculate the ratio of  $\text{Ni}^{2+}/\text{Ni}^{3+}$  in this La-dominated region.

Ni-3p core-level spectrums could be used to distinguish  $\text{Ni}^{2+}$  and  $\text{Ni}^{3+}$ , which are shown in Figure 6a,b for undoped and Sr-doped  $\text{LaNiO}_{3-\sigma}$ , respectively. Shirley background and Lorentzian-Gaussian mixed function were used to ensure the quality of the peak fitting. It is consistent with the previous research that the peaks at 66.08 eV and 71.08 eV could be attributed to  $\text{Ni}^{2+}$  3p<sub>3/2</sub> and  $\text{Ni}^{3+}$  3p<sub>3/2</sub>, respectively. The ratio of  $\text{Ni}^{2+}$ :

$\text{Ni}^{3+}$  can be calculated, which are 84.83:15.17 and 89.86:10.14 for undoped and Sr-doped  $\text{LaNiO}_{3-\sigma}$ , respectively. In these samples, La belongs to +3 valance and Sr belongs to +2 valance; therefore, the oxygen vacancy content  $\sigma$  can be calculated, and the results are shown in Table 1. To sum up, the exact chemical formulas are respectively  $\text{LaNiO}_{2.58}$  ( $\sigma = 0.42$ ) and  $\text{La}_{0.875}\text{Sr}_{0.125}\text{NiO}_{2.49}$  ( $\sigma = 0.51$ ), which indicates that Sr-doping can introduce more oxygen vacancy into  $\text{LaNiO}_3$ .

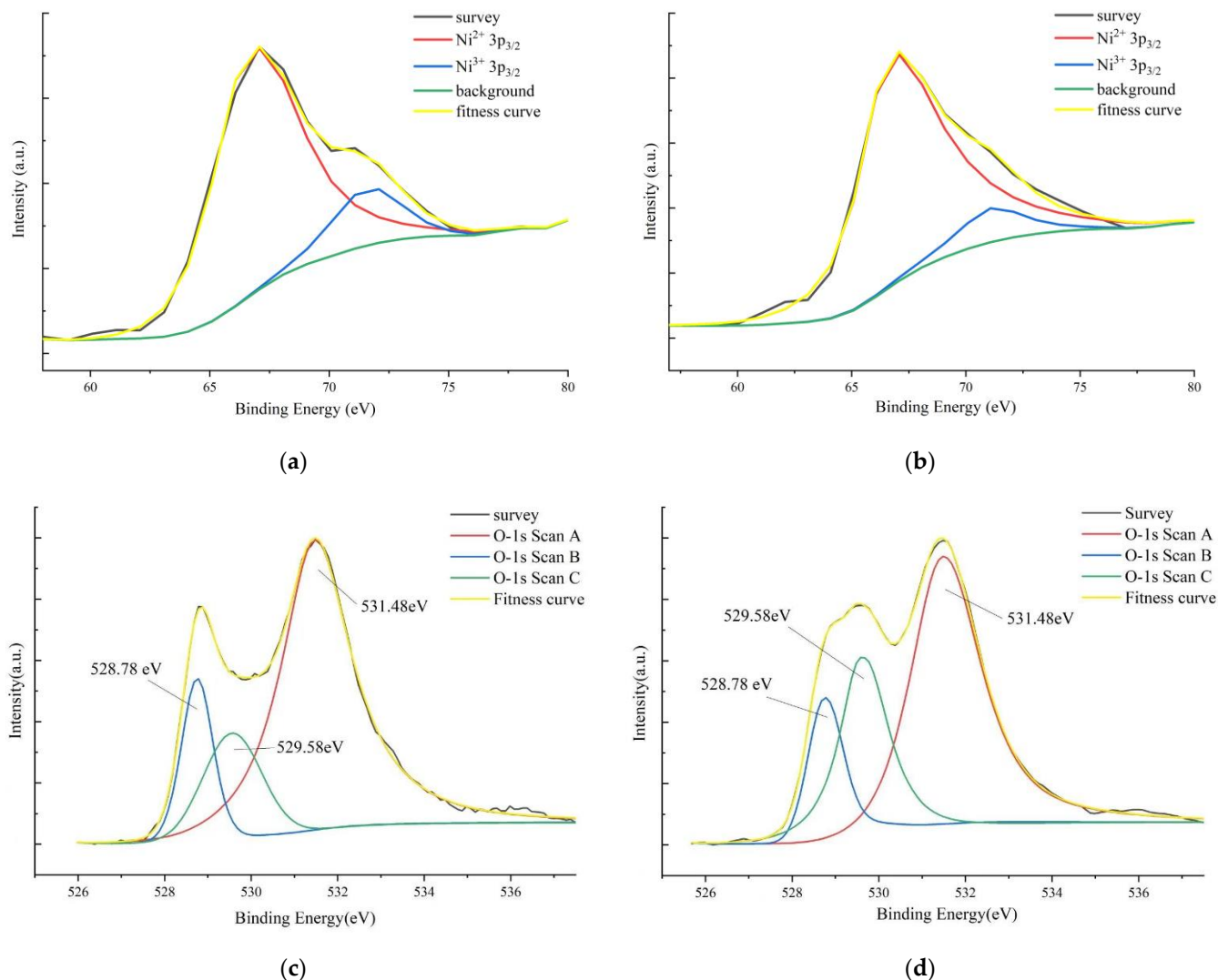


**Figure 6.** XPS spectrum of undoped and Sr-doped  $\text{LaNiO}_{3-\sigma}$ . (a,b) Ni-3p scan; (c,d) O-1s scan.

**Table 1.** Calculation results of the ratio of  $\text{Ni}^{2+}:\text{Ni}^{3+}$  and oxygen vacancy content  $\sigma$ .

Sample	$\text{Ni}^{2+}:\text{Ni}^{3+}$	Sr Percentage (%)	$\sigma$
$\text{LaNiO}_{3-\sigma}$	84.83:15.17	0	0.42
$\text{La}_{0.875}\text{Sr}_{0.125}\text{NiO}_{3-\sigma}$	89.86:10.14	12.5	0.51

The spectrums of O-1s are shown in Figure 6c,d. In the O-1s region, there are three wide symmetric peaks, which are 528.78 eV, 529.58 eV, and 531.48 eV, respectively. The 528.78 eV peak is attributed to the  $\text{O}^{2-}$  ion on the rhombohedral  $\text{LaNiO}_3$  array perovskite structure, and the Ni atom is completely supplemented by the nearest  $\text{O}^{2-}$  ion. Therefore, the peak O-1s spectrum at 528.78 eV can be attributed to lattice oxygen. In the meanwhile, the higher binding energy is assigned to chemisorbed oxygen at 529.58 eV, and the highest binding energy is assigned to physically-adsorbed oxygen at 531.48 eV [45–47].

In Figure 6d, it can be observed that, compared with undoped  $\text{LaNiO}_{3-\sigma}$ , the lattice oxygen content of Sr-doped is reduced, and the chemisorbed oxygen content on the sample surface is increased. Therefore, Sr-doping can introduce more oxygen vacancy into perovskite and significantly improve the adsorption of oxygen molecules on the surface of Sr-doped  $\text{LaNiO}_{3-\sigma}$ , enhancing the photocatalytic performance of  $\text{LaNiO}_{3-\sigma}$ .

### 2.3. Photocatalytic Performance

The photocatalytic properties of the undoped and Sr-doped  $\text{LaNiO}_{3-\sigma}$  samples were investigated by simulating the photodegradation of methyl orange (MO) solution under solar irradiation. In addition, the MO adsorption (%) on the undoped and Sr-doped  $\text{LaNiO}_{3-\sigma}$  samples was investigated by radicals trapping experiments under a dark environment.

As shown in Figure 7a,  $A_t/A_0$  is the ratio of MO concentration under the dark environment with no photocatalytic reaction. After stirring for 25 min, the adsorption and desorption on the undoped and Sr-doped  $\text{LaNiO}_{3-\sigma}$  are balanced. MO adsorption percentage of undoped  $\text{LaNiO}_{3-\sigma}$  is 3.2%, which is much lower than that of Sr-doped  $\text{LaNiO}_{3-\sigma}$  (26.1%). Figure 7b shows that  $C_t/C_0$  is the ratio of MO concentration under the simulated solar irradiation, while photocatalyst is added into the reaction solution under the simulated solar irradiation. The photocatalytic degradation rates of the undoped and Sr-doped  $\text{LaNiO}_{3-\sigma}$  samples to MO are different. After irradiation for 80 min, the fraction of degraded MO solution was 92% and 100% for undoped and Sr-doped  $\text{LaNiO}_{3-\sigma}$ , respectively.

It is obvious that Sr-doped  $\text{LaNiO}_3$  has higher photocatalytic performance than undoped  $\text{LaNiO}_{3-\sigma}$ . Figure 7c shows the apparent reaction rate constants ( $k$ ) for the degradation of MO. According to the fitted kinetic constant, the degradation rate constants of MO catalyzed by undoped and Sr-doped  $\text{LaNiO}_{3-\sigma}$  are  $-0.03245 \text{ min}^{-1}$  and  $-0.05217 \text{ min}^{-1}$ , respectively. One of the reasons is that the more oxygen vacancy on the surface, the more active sites provided by the exposed surface, and oxygen vacancy can inhibit the photogenerated electron-hole pair recombination. Another reason is band gap width of the energy band structure of  $\text{LaNiO}_{3-\sigma}$  becomes narrower, which would change the light response range wider. Therefore, oxygen vacancy of  $\text{LaNiO}_{3-\sigma}$  can be introduced more by doping lower valence element at A site to improve the photocatalytic performance of  $\text{LaNiO}_{3-\sigma}$ .

### 2.4. First-Principle Calculations

To investigate how oxygen vacancy has impacts on the band structure and density of states, four different kinds of supercell are built in Material Studio, including  $\text{LaNiO}_3$ ,  $\text{LaNiO}_{3-\sigma}$ ,  $\text{La}_{0.875}\text{Sr}_{0.125}\text{NiO}_3$ , and  $\text{La}_{0.875}\text{Sr}_{0.125}\text{NiO}_{3-\sigma}$ .  $\text{LaNiO}_3$  and  $\text{La}_{0.875}\text{Sr}_{0.125}\text{NiO}_3$  mean that there is no vacancy in the supercell. On the contrary,  $\text{LaNiO}_{3-\sigma}$  and  $\text{La}_{0.875}\text{Sr}_{0.125}\text{NiO}_{3-\sigma}$  mean there is oxygen vacancy in the supercell.

According to the XRD results of the prepared  $\text{LaNiO}_3$ , the crystal phase of  $\text{LaNiO}_3$  is R-3c rhombohedral space group, as shown in Figure 8a, and the unit cell contains 10 calculated atoms, so all the first-principle calculations are based on this structure. A model of  $\text{LaNiO}_3$  was built, which is a  $2 \times 2 \times 1$  supercell of the R-3c space group, as shown in Figure 8b, while the periodical extra Ni atoms were removed. Meanwhile, Figure 8c is the top view of the  $\text{LaNiO}_3$   $2 \times 2 \times 1$  supercell containing 40 atoms. Based on the  $\text{LaNiO}_3$   $2 \times 2 \times 1$  supercell, the La atom on the 1-position was substituted by the Sr atom, and the O atom on the 2-position was removed, so  $\text{La}_{0.875}\text{Sr}_{0.125}\text{NiO}_{3-\sigma}$   $2 \times 2$  supercell s built as shown in Figure 8d, while  $\text{LaNiO}_{3-\sigma}$  and  $\text{La}_{0.875}\text{Sr}_{0.125}\text{NiO}_3$  are also built but not shown.

#### 2.4.1. Band Structure

As shown in Figure 9, according to First-principle, the calculation results of the four kinds of supercells show that the band gap width is 2.975 eV, 2.599 eV, 2.284 eV, and 2.074 eV for  $\text{LaNiO}_3$ ,  $\text{LaNiO}_{3-\sigma}$ ,  $\text{La}_{0.875}\text{Sr}_{0.125}\text{NiO}_3$ , and  $\text{La}_{0.875}\text{Sr}_{0.125}\text{NiO}_{3-\sigma}$ , respectively. It can be observed that compared with  $\text{LaNiO}_3$ , the conduction band level of  $\text{LaNiO}_{3-\sigma}$  decreases, which leads to a narrower band gap width. The same situation occurs in  $\text{La}_{0.875}\text{Sr}_{0.125}\text{NiO}_3$ , whose band gap width is even smaller than that of  $\text{LaNiO}_{3-\sigma}$ . Moreover,



$\text{La}_{0.875}\text{Sr}_{0.125}\text{NiO}_{3-\sigma}$  obtained the smallest band gap width among the four supercell crystals under the combined action of oxygen vacancy and Sr element. The introduction of oxygen vacancy and Sr-doping will lead to the narrowing of the band gap width of  $\text{LaNiO}_3$  so as to obtain a wider light response range. The simulated band gap width of complete  $\text{LaNiO}_3$  is 2.975 eV, which is quite close to the experimental result of 3.010 eV by Aamir Ghafoor et al. [24].

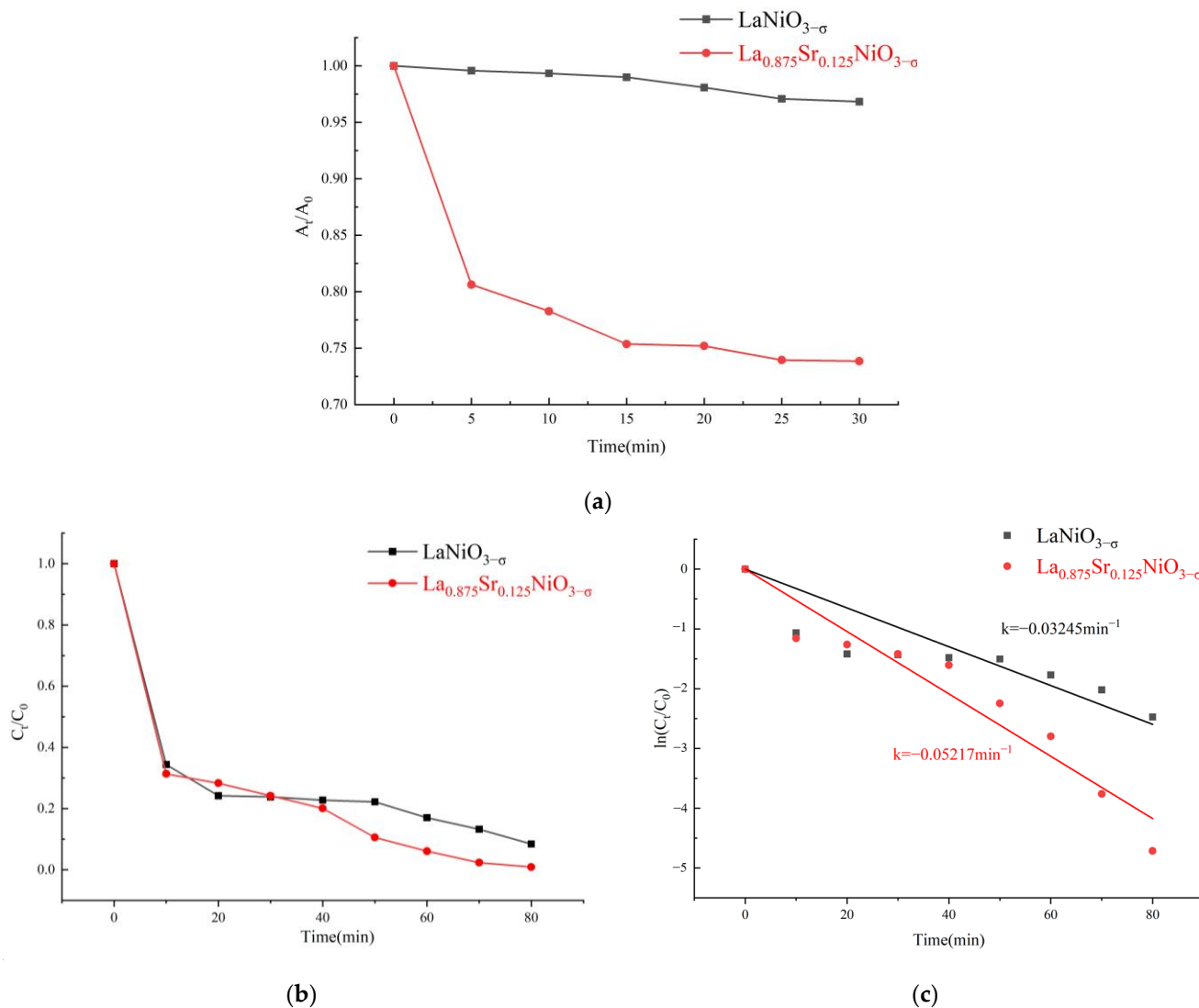


**Figure 7.** Adsorption curves (a) under a dark environment; degradation curves (b) and kinetic curves (c) of MO catalyzed by undoped and Sr-doped  $\text{LaNiO}_{3-\sigma}$  under the simulated solar irradiation.

Compared with  $\text{LaNiO}_3$ , as shown in Figure 9a, new energy levels appear in the band structure of the other three supercells nearby the Fermi level, which might be caused by Sr-doping or oxygen vacancy. The density of states is necessarily calculated to explore the main reason for the band structure changes. As shown in Figure 9b–d, there are three energy levels in the band gap, which is not intensive in the band structure. Oxygen vacancy and Sr-doping could lead to the generation of the three sparse and new energy levels, which would not be regarded as conduction bands or valence bands [41].

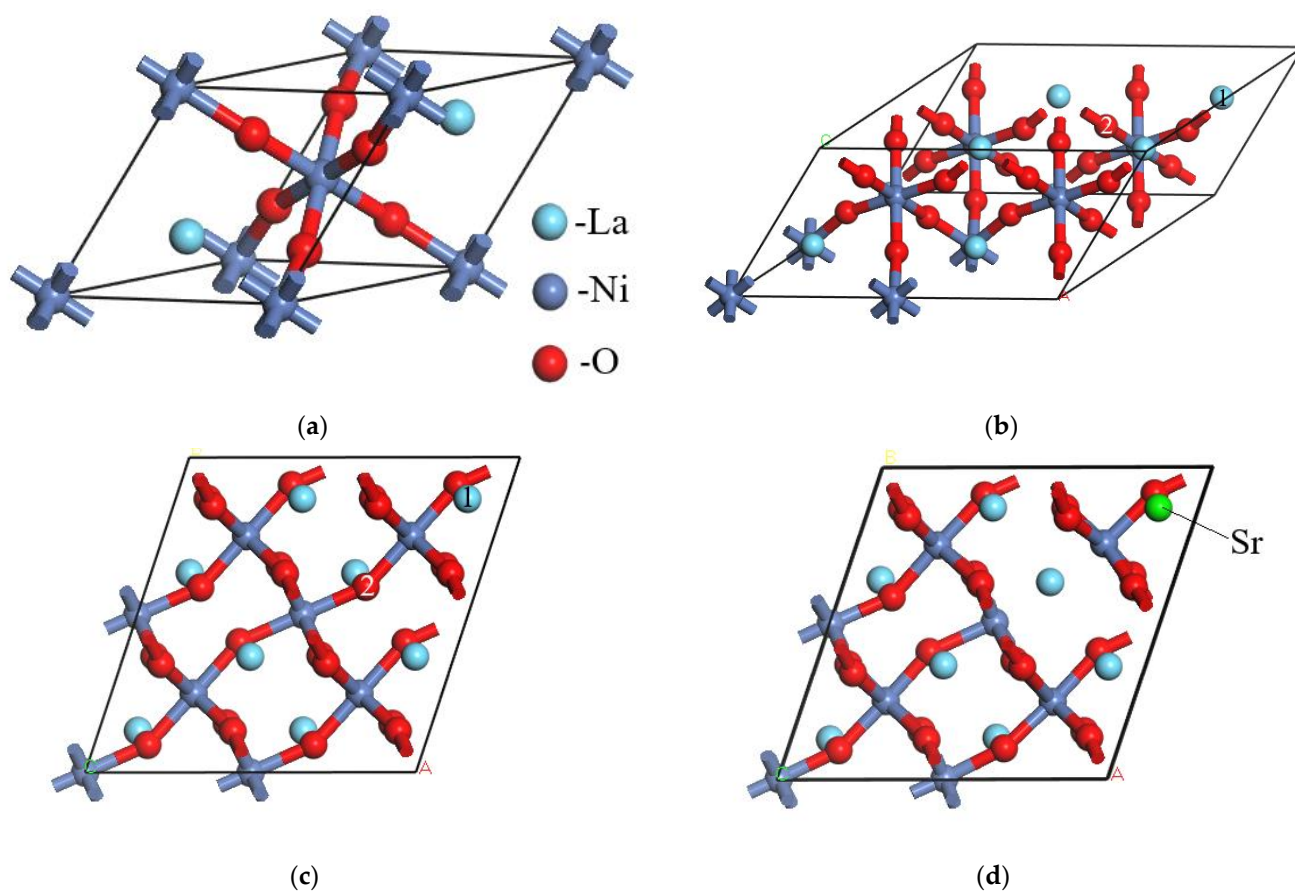


**Figure 8.** (a)  $\text{LaNiO}_3$  primitive unit cell; (b)  $\text{LaNiO}_3$   $2 \times 2 \times 1$  supercell; (c)  $\text{LaNiO}_3$   $2 \times 2 \times 1$  supercell top view; (d)  $\text{La}_{0.875}\text{Sr}_{0.125}\text{NiO}_{3-\sigma}$   $2 \times 2 \times 1$  supercell top view; 1: substitution position, 2: oxygen vacancy position.

#### 2.4.2. Density of States

The calculation of the density of states is helpful in analyzing the composition of conduction and valence bands in the band structure of the supercells. Figure 10a shows the density of states (DOS) and partial density of state (PDOS) of the complete  $\text{LaNiO}_3$  supercell in the range of  $-10 \sim 20$  eV. It can be observed that the conduction band of  $\text{LaNiO}_3$  is mainly composed of d orbitals in the range of  $-8 \sim 0$  eV, and the valence band is composed of p orbits and d orbits in the range of  $0 \sim 10$  eV, while there is too high energy level in s orbits.

As shown in Figure 10b, the density of states of the four supercells can indicate the changes in the band structure. Compared with  $\text{LaNiO}_3$ , the density of states of  $\text{LaNiO}_{3-\sigma}$  globally shifts to the direction of the lower energy level. The same situation occurs in the group of  $\text{La}_{0.875}\text{Sr}_{0.125}\text{NiO}_3$  and  $\text{La}_{0.875}\text{Sr}_{0.125}\text{NiO}_{3-\sigma}$ . It can be observed that the appearance of oxygen vacancy will lead the spectrum shifts to the direction of the lower energy level globally, and new energy levels are generated near the Fermi level. Moreover, according to the comparison of  $\text{LaNiO}_3$  and  $\text{La}_{0.875}\text{Sr}_{0.125}\text{NiO}_3$ , Sr-doping can also cause the generation of new energy levels near the Fermi level. In addition, the DOS of the new energy levels is too small to be attributed to the conduction band or valence band [41]. In general, oxygen vacancy and Sr-doping could lead to the narrowing of the band gap width of  $\text{LaNiO}_3$ , which is consistent with the calculation results of the band structure. In addition, both oxygen vacancy and Sr-doping can lead to the generation of new energy levels near the Fermi level.

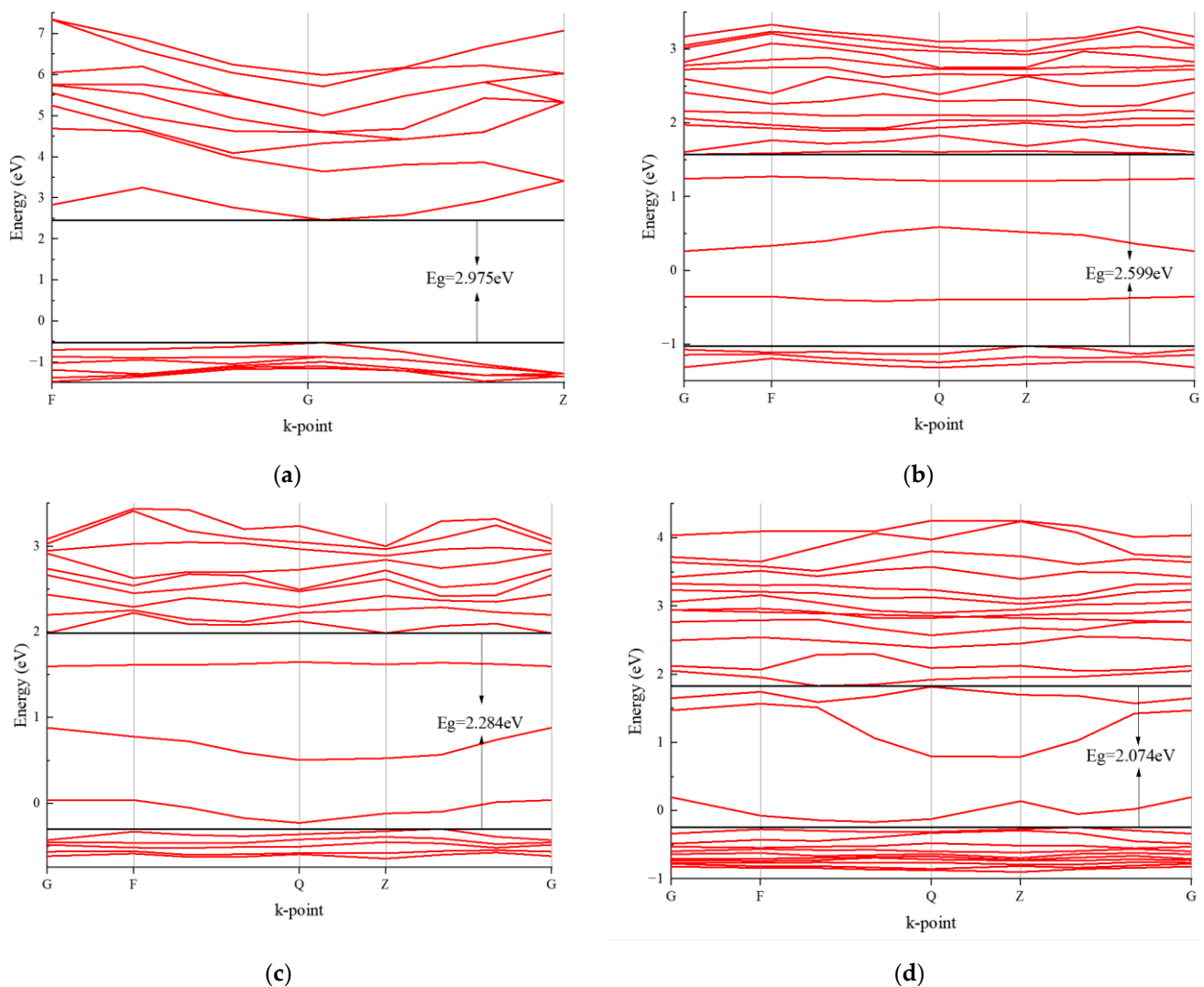


**Figure 9.** Band structure near the Fermi level. (a)  $\text{LaNiO}_3$ ; (b)  $\text{LaNiO}_{3-\sigma}$ ; (c)  $\text{La}_{0.875}\text{Sr}_{0.125}\text{NiO}_3$ ; (d)  $\text{La}_{0.875}\text{Sr}_{0.125}\text{NiO}_{3-\sigma}$ .

The results of the partial density of states are shown in Figure 11. It is observed that the valance band in the range of  $-8\sim 0$  eV is mainly composed of O-2p and Ni-3d orbits, while the conduction band in the range of  $0\sim 10$  eV is mainly composed of Ni-3d and La-3d orbits. Moreover, the introduction of oxygen vacancy causes the O-2p and Ni-3d orbitals to generate new energy levels near the Fermi level and all PDOS to shift globally toward lower energy levels. As shown in Figure 11d, the Sr-3d orbit didn't generate new energy levels near the Fermi levels. However, Sr-doping promotes O-2p and Ni-3d to generate new energy levels near the Fermi level, which is also the reason why the band gap width of  $\text{La}_{0.875}\text{Sr}_{0.125}\text{NiO}_3$  supercell becomes narrower.

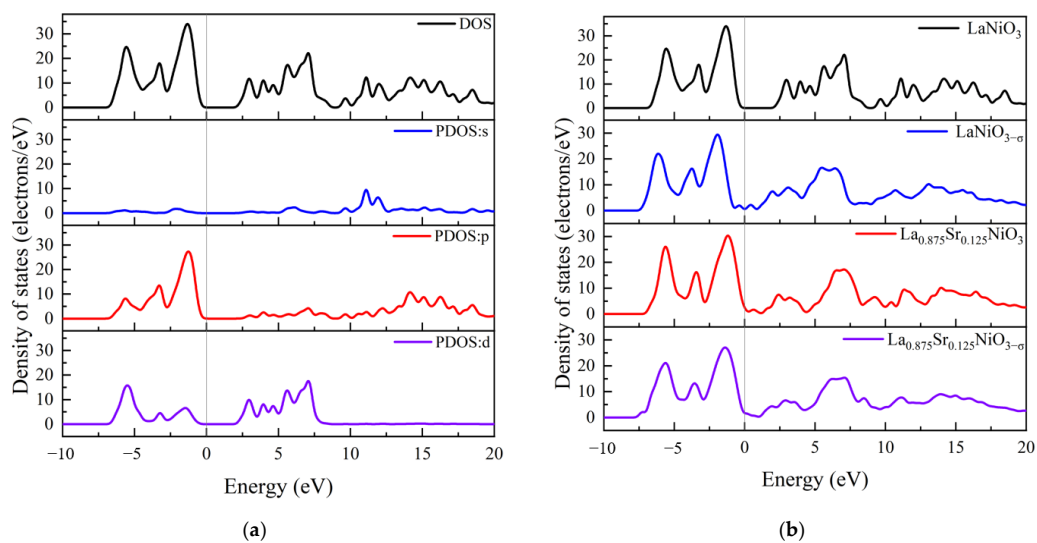


**Figure 10.** (a) The density of state and partial density of state of LaNiO<sub>3</sub>; (b) Density of state of four supercells.

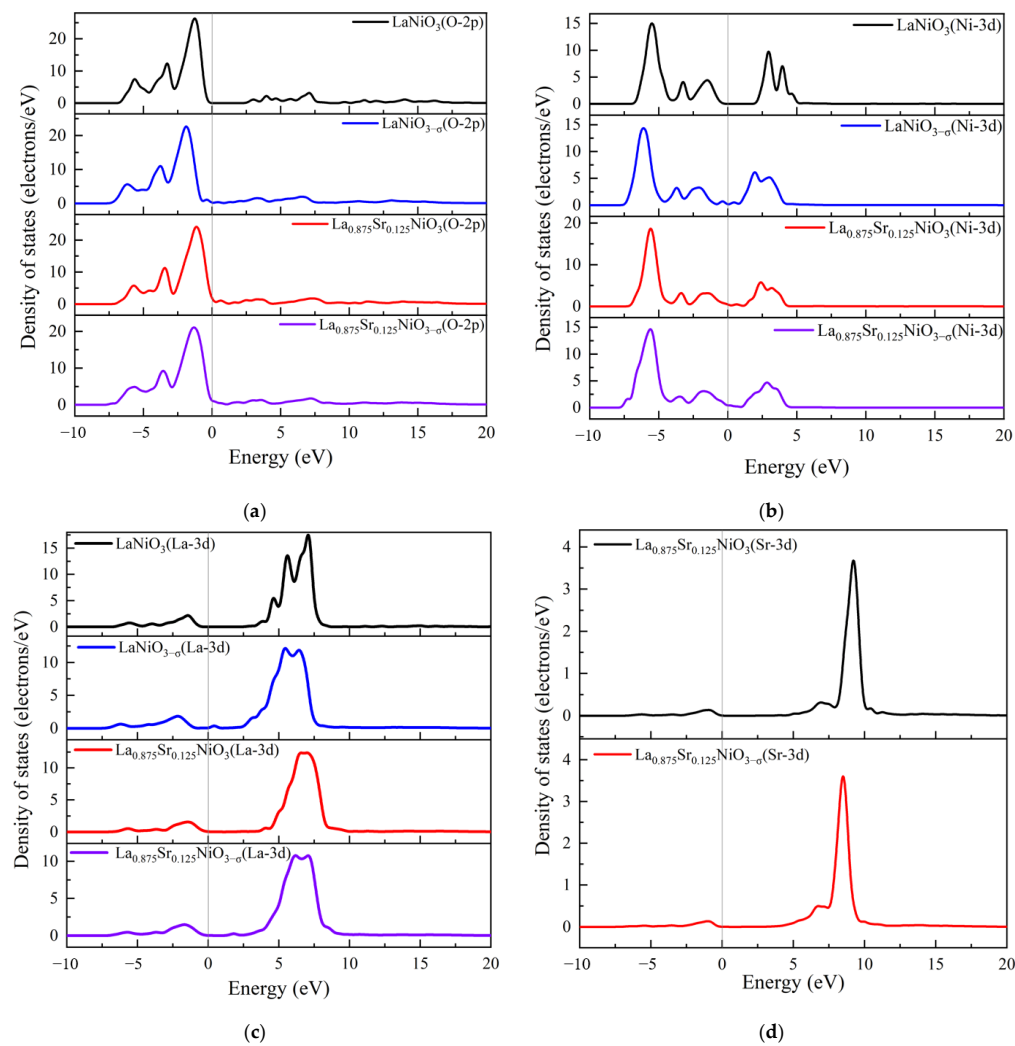


**Figure 11.** Partial density of states. (a) O-2p; (b) Ni-3d; (c) La-3d; (d) Sr-3d.

### 3. Materials and Methods

#### 3.1. Materials

Lanthanum nitrate hexahydrate ( $\text{La}(\text{NO}_3)_3 \cdot 6\text{H}_2\text{O}$ , CAS: 10277-43-7), Strontium acetate ( $\text{Sr}(\text{CH}_2\text{COOH})_2$ , CAS: 543-94-2), Nickel acetate tetrahydrate ( $\text{Ni}(\text{CH}_2\text{COOH})_2 \cdot 4\text{H}_2\text{O}$ , CAS: 6018-89-9), Citric acid ( $\text{C}_6\text{H}_8\text{O}_7$ , CAS: 77-92-9) and Methyl orange ( $\text{C}_{14}\text{H}_{14}\text{N}_3\text{SO}_3\text{Na}$ , CAS: 547-58-0) were purchased from Macklin (Shanghai, China). All chemicals were reagent grade and used as received.

#### 3.2. Preparation and Characterization

$\text{LaNiO}_{3-\sigma}$  and  $\text{La}_{1-x}\text{Sr}_x\text{NiO}_{3-\sigma}$  ( $x = 0.125$ ) were prepared by the sol-gel method [48].  $\text{La}(\text{NO}_3)_3 \cdot 6\text{H}_2\text{O}$ ,  $\text{Ni}(\text{CH}_2\text{COOH})_2 \cdot 4\text{H}_2\text{O}$ , and citric acid were dissolved in deionized water and stirred according to the stoichiometric ratio of 1:1:1.5 to prepare undoped  $\text{LaNiO}_{3-\sigma}$ . After the raw material was completely dissolved, ammonia water was added to adjust the pH value of the solution to 8.0. Then the solution was placed in a water bath at 80 °C for 3 h, and the clear solution gradually turned into a viscous gel. The gel was put into a thermostatic drying oven at 150 °C for 24 h to obtain the dry gel. The dry gel was put into a crucible and calcined in a muffle furnace at 700 °C for 4 h. The calcined products were ground into a powder with an agate mortar.  $\text{La}(\text{NO}_3)_3 \cdot 6\text{H}_2\text{O}$ ,  $\text{Sr}(\text{CH}_2\text{COOH})_2$ ,  $\text{Ni}(\text{CH}_2\text{COOH})_2 \cdot 4\text{H}_2\text{O}$ , and citric acid were dissolved in deionized water for stirring according to the stoichiometric ratio of  $1-x:x:1:1.5$  to prepare  $\text{La}_{0.875}\text{Sr}_{0.125}\text{NiO}_{3-\sigma}$ , followed by the same steps as the former preparation.

X-ray diffractometer (Bruker, Billerica, MA, USA) was used to characterize the crystal structure of the powder sample, using Bruker D8 Advance model, Cu K $\alpha$  radiation ( $\lambda = 1.54056 \text{ \AA}$ ) and  $2\theta$  scanning range from 20° to 80°.

Field emission scanning electron microscopy (Zeiss, Oberkochen, Germany) is used to characterize the microscopic appearance of the prepared samples using the Merlin SU8200 model.

X-ray photoelectron spectroscopy (Kratos, Manchester, UK) is used to characterize the elemental composition qualitative analysis and elemental valence analysis on the sample surface, using Axis Ultra DLD type.

#### 3.3. Photocatalytic Performance Test

The photocatalytic performance of the samples was studied by photocatalytic degradation of methyl orange. Firstly, a sample of 100 mL methyl orange solution with a concentration of 10 mg/L was taken as  $C_0$ , and then a 250 mg photocatalyst sample was added. Then, a long arc xenon lamp (GXZ500) was used as the simulated solar illumination. The solution system was photocatalyzed under this condition, and samples were taken every 10 min. The degraded solution was analyzed by Shimadzu UV-2700 UV-visible spectrophotometer (Shimadzu, Kyoto, Japan), and the concentration of methyl orange after degradation was detected at a wavelength of 463 nm.

MO adsorption (%) on the undoped and Sr-doped  $\text{LaNiO}_{3-\sigma}$  were studied by radicals trapping experiments under a dark environment. A sample of 100 mL methyl orange solution with a concentration of 10 mg/L was taken as  $A_0$ , and then a 250 mg photocatalyst sample was added. After stirring for 25 min, the equilibrium of adsorption and desorption between dye and photocatalyst was achieved.

#### 3.4. First-Principle Calculations

All first-principle calculations are studied by the Cambridge Serial Total Energy Package (CASTEP) module [49] in Material Studio. According to first-principle calculations and generalized gradient approximation of Perdew Burke Ernzerhof exchange-correlation functional (GGA-PBE) [50], the ultra-soft pseudopotential (USPP) system [51] was used to describe the interaction between electrons and ions accurately. The calculation results of the models include band structure and density of states of the  $\text{LaNiO}_3$  rhombohedral perovskite (R-3c). All calculations are based on the truncation energy of 520 eV and the grid

distribution of K points of  $2 \times 2 \times 1$  in Brillouin space [52]. The parameters of structural optimization are set as follows: the convergence accuracy of energy is  $5.0 \times 10^{-5}$  eV/Atom, the convergence accuracy of atomic force is  $0.1$  eV/Å, and the convergence accuracy of atomic displacement is  $0.005$  Å.

#### 4. Conclusions

In this study,  $\text{LaNiO}_{3-\sigma}$  and  $\text{La}_{0.875}\text{Sr}_{0.125}\text{NiO}_{3-\sigma}$  were successfully prepared by the sol-gel method, and the crystal phases were R-3c space group of the rhombohedral system shown by XRD results. It can be observed that the undoped and Sr-doped  $\text{LaNiO}_{3-\sigma}$  powders crystallized well under the predetermined experimental conditions, and the powder particles have formed agglomerates partially in the SEM images. XPS analysis results confirmed that the Sr-doping method could introduce more oxygen vacancy in  $\text{LaNiO}_{3-\sigma}$ , which is consistent with the design idea of the experiment. In addition, oxygen vacancy contents  $\sigma$  are 0.42 and 0.51 for  $\text{LaNiO}_{3-\sigma}$  and  $\text{La}_{0.875}\text{Sr}_{0.125}\text{NiO}_{3-\sigma}$ , respectively. Radicals trapping experiments under a dark environment show that the MO adsorption percentage of Sr-doped  $\text{LaNiO}_{3-\sigma}$  (26.1%) is much larger than that of undoped  $\text{LaNiO}_{3-\sigma}$  (3.2%) after stirring for 25 min. According to MO degradation curves and kinetic curves, the MO degradation rate of Sr-doped  $\text{LaNiO}_{3-\sigma}$  (100%) is larger than that of undoped  $\text{LaNiO}_{3-\sigma}$  (92%) for a degradation time of 80 min. First-principle calculation results show that the valence band in the range of  $-8\sim 0$  eV is mainly composed of O-2p and Ni-3d orbits, while the conduction band in the range of  $0\sim 10$  eV is mainly composed of Ni-3d and La-3d orbits. In addition, oxygen vacancy and Sr-doping can lead to the generation of new energy levels near the Fermi level and the narrowing of the band gap of  $\text{LaNiO}_3$ . These results verify that  $\text{LaNiO}_{3-\sigma}$  with more oxygen vacancy can be successfully prepared by the Sr-doping method according to the conservation of valence so that the photocatalytic performance of  $\text{LaNiO}_{3-\sigma}$  can be improved.

**Author Contributions:** Conceptualization, L.G.; data curation, Y.Z.; funding acquisition, Q.Z., J.L. and Q.M.; methodology, Q.X.; writing—original draft, Y.Z.; Writing—review & editing, Y.Z. All authors have read and agreed to the published version of the manuscript.

**Funding:** This research was funded by the Department of Science and Technology of Guangdong Province (2018B030323017); Key-Area Research and Development Program of Guangdong Province (2020B090922006); Science and Technology Program of Guangzhou (2019050001); National Natural Science Foundation of China (62005081).

**Data Availability Statement:** Not applicable.

**Conflicts of Interest:** The authors declare no conflict of interest.

#### References

1. Fujishima, A.; Honda, K. Electrochemical photolysis of water at a semiconductor electrode. *Nature* **1972**, *238*, 37–38. [[CrossRef](#)] [[PubMed](#)]
2. Pena, M.; Fierro, J. Chemical structures and performance of perovskite oxides. *Chem. Rev.* **2001**, *101*, 1981–2018. [[CrossRef](#)] [[PubMed](#)]
3. Xu, Y.-F.; Yang, M.-Z.; Chen, B.-X.; Wang, X.-D.; Chen, H.-Y.; Kuang, D.-B.; Su, C.-Y. A CsPbBr<sub>3</sub> perovskite quantum dot/graphene oxide composite for photocatalytic CO<sub>2</sub> reduction. *J. Am. Chem. Soc.* **2017**, *139*, 5660–5663. [[CrossRef](#)] [[PubMed](#)]
4. Yang, E.-h.; Noh, Y.S.; Hong, G.H.; Moon, D.J. Combined steam and CO<sub>2</sub> reforming of methane over La<sub>1-x</sub>Sr<sub>x</sub>NiO<sub>3</sub> perovskite oxides. *Catal. Today* **2018**, *299*, 242–250. [[CrossRef](#)]
5. Bhosale, S.S.; Kharade, A.K.; Jokar, E.; Fathi, A.; Chang, S.-M.; Diao, E.W.-G. Mechanism of photocatalytic CO<sub>2</sub> reduction by bismuth-based perovskite nanocrystals at the gas–solid interface. *J. Am. Chem. Soc.* **2019**, *141*, 20434–20442. [[CrossRef](#)]
6. Kumar, S.; Regue, M.; Isaacs, M.A.; Freeman, E.; Eslava, S. All-inorganic CsPbBr<sub>3</sub> nanocrystals: Gram-scale mechanochemical synthesis and selective photocatalytic CO<sub>2</sub> reduction to methane. *ACS Appl. Energy Mater.* **2020**, *3*, 4509–4522. [[CrossRef](#)]
7. Shyamal, S.; Dutta, S.K.; Das, T.; Sen, S.; Chakraborty, S.; Pradhan, N. Facets and defects in perovskite nanocrystals for photocatalytic CO<sub>2</sub> reduction. *J. Phys. Chem. Lett.* **2020**, *11*, 3608–3614. [[CrossRef](#)]
8. Bui, D.-N.; Mu, J.; Wang, L.; Kang, S.-Z.; Li, X. Preparation of Cu-loaded SrTiO<sub>3</sub> nanoparticles and their photocatalytic activity for hydrogen evolution from methanol aqueous solution. *Appl. Surf. Sci.* **2013**, *274*, 328–333. [[CrossRef](#)]

9. Kim, I.S.; Pellin, M.J.; Martinson, A.B. Acid-compatible halide perovskite photocathodes utilizing atomic layer deposited TiO<sub>2</sub> for solar-driven hydrogen evolution. *ACS Energy Lett.* **2019**, *4*, 293–298. [[CrossRef](#)]
10. Zhang, H.; Chen, G.; He, X.; Xu, J. Electronic structure and photocatalytic properties of Ag–La codoped CaTiO<sub>3</sub>. *J. Alloys Compd.* **2012**, *516*, 91–95. [[CrossRef](#)]
11. Mao, M.; Xu, J.; Li, L.; Zhao, S.; Li, X.; Li, Y.; Liu, Z. High performance hydrogen production of MoS<sub>2</sub>-modified perovskite LaNiO<sub>3</sub> under visible light. *Ionics* **2019**, *25*, 4533–4546. [[CrossRef](#)]
12. Huerta-Flores, A.M.; Sánchez-Martínez, D.; del Rocío Hernández-Romero, M.; Zarazua-Morin, M.E.; Torres-Martínez, L.M. Visible-light-driven BaBiO<sub>3</sub> perovskite photocatalysts: Effect of physicochemical properties on the photoactivity towards water splitting and the removal of rhodamine B from aqueous systems. *J. Photochem. Photobiol. A Chem.* **2019**, *368*, 70–77. [[CrossRef](#)]
13. Xiao, G.; Liu, Q.; Wang, S.; Komvokis, V.G.; Amiridis, M.D.; Heyden, A.; Ma, S.; Chen, F. Synthesis and characterization of Mo-doped SrFeO<sub>3–δ</sub> as cathode materials for solid oxide fuel cells. *J. Power Sources* **2012**, *202*, 63–69. [[CrossRef](#)]
14. Huang, Y.-H.; Dass, R.I.; Xing, Z.-L.; Goodenough, J.B. Double perovskites as anode materials for solid-oxide fuel cells. *Science* **2006**, *312*, 254–257. [[CrossRef](#)] [[PubMed](#)]
15. Afroze, S.; Karim, A.; Cheok, Q.; Eriksson, S.; Azad, A.K. Latest development of double perovskite electrode materials for solid oxide fuel cells: A review. *Front. Energy* **2019**, *13*, 770–797. [[CrossRef](#)]
16. Huang, Y.-H.; Liang, G.; Croft, M.; Lehtimäki, M.; Karppinen, M.; Goodenough, J.B. Double-perovskite anode materials Sr<sub>2</sub>MMoO<sub>6</sub> (M = Co, Ni) for solid oxide fuel cells. *Chem. Mater.* **2009**, *21*, 2319–2326. [[CrossRef](#)]
17. Li, F.-T.; Liu, Y.; Liu, R.-H.; Sun, Z.-M.; Zhao, D.-S.; Kou, C.-G. Preparation of Ca-doped LaFeO<sub>3</sub> nanopowders in a reverse microemulsion and their visible light photocatalytic activity. *Mater. Lett.* **2010**, *64*, 223–225. [[CrossRef](#)]
18. Wang, Y.; Ma, W.; Song, Y.; Chen, J.; Xu, J.; Wang, D.; Mao, Z. Enhanced photocatalytic performance of SrTiO<sub>3</sub> powder induced by europium dopants. *J. Rare Earths* **2021**, *39*, 541–547. [[CrossRef](#)]
19. Shah, A.A.; Ahmad, S.; Azam, A. Investigation of structural, optical, dielectric and magnetic properties of LaNiO<sub>3</sub> and LaNi<sub>1–x</sub>MxO<sub>3</sub> (M = Fe, Cr & Co; x = 5%) nanoparticles. *J. Magn. Magn. Mater.* **2020**, *494*, 165812.
20. Jayapandi, S.; Prakasini, V.A.; Anitha, K. Ag modified LaCoO<sub>3</sub> perovskite oxide for photocatalytic application. In Proceedings of the AIP Conference Proceedings, Maharashtra, India, 5–6 July 2018; p. 140048. [[CrossRef](#)]
21. Chen, L.; Pradhan, S. Low temperature synthesis of metal doped perovskites catalyst for hydrogen production by autothermal reforming of methane. *Int. J. Hydrog. Energy* **2016**, *41*, 14605–14614. [[CrossRef](#)]
22. Zhang, W.; Du, L.; Bi, F.; He, H. A novel SrTiO<sub>3</sub>/HZSM-5 photocatalyst prepared by sol–gel method. *Mater. Lett.* **2015**, *157*, 103–105. [[CrossRef](#)]
23. Moraes Júnior, E.; Leite, J.; Santos, A.; Souza, M.; Pedrosa, A. Nickel-based perovskite catalysts: Synthesis and catalytic tests in the production of syngas. *Cerâmica* **2018**, *64*, 436–442. [[CrossRef](#)]
24. Ghafoor, A.; Bibi, I.; Ata, S.; Majid, F.; Kamal, S.; Iqbal, M.; Iqbal, S.; Noureen, S.; Basha, B.; Alwadai, N. Energy band gap tuning of LaNiO<sub>3</sub> by Gd, Fe and Co ions doping to enhance solar light absorption for efficient photocatalytic degradation of RhB dye: A mechanistic approach. *J. Mol. Liq.* **2021**, *343*, 117581. [[CrossRef](#)]
25. Wei, K.; Faraj, Y.; Yao, G.; Xie, R.; Lai, B. Strategies for improving perovskite photocatalysts reactivity for organic pollutants degradation: A review on recent progress. *Chem. Eng. J.* **2021**, *414*, 128783. [[CrossRef](#)]
26. Rehman, S.U.; Shaur, A.; Song, R.-H.; Lim, T.-H.; Hong, J.-E.; Park, S.-J.; Lee, S.-B. Nano-fabrication of a high-performance LaNiO<sub>3</sub> cathode for solid oxide fuel cells using an electrochemical route. *J. Power Sources* **2019**, *429*, 97–104. [[CrossRef](#)]
27. Yu, Z.; Gao, L.; Yuan, S.; Zhu, Y. Solid defect structure and catalytic activity of perovskite-type catalysts La<sub>1–x</sub>Sr<sub>x</sub>NiO<sub>3–λ</sub> and La<sub>1–1.333x</sub>Th<sub>x</sub>NiO<sub>3–λ</sub>. *J. Chem. Soc. Faraday Trans.* **1992**, *88*, 3245–3249. [[CrossRef](#)]
28. Kagomiya, I.; Jimbo, K.; Kakimoto, K.-i. Distribution change of oxygen vacancies in layered perovskite type (Sr, La)<sub>n+1</sub>Fe<sub>n</sub>O<sub>3n+1</sub> (n = 3). *J. Solid State Chem.* **2013**, *207*, 184–189. [[CrossRef](#)]
29. Guan, L.; Liu, B.; Jin, L.; Guo, J.; Zhao, Q.; Wang, Y.; Fu, G. Electronic structure and optical properties of LaNiO<sub>3</sub>: First-principles calculations. *Solid State Commun.* **2010**, *150*, 2011–2014. [[CrossRef](#)]
30. Malashevich, A.; Ismail-Beigi, S. First-principles study of oxygen-deficient LaNiO<sub>3</sub> structures. *Phys. Rev. B* **2015**, *92*, 144102. [[CrossRef](#)]
31. Zhang, B.; Liu, P.; Li, Z.; Song, X. Synthesis of two-dimensional Sr-doped LaNiO<sub>3</sub> nanosheets with improved electrochemical performance for energy storage. *Nanomaterials* **2021**, *11*, 155. [[CrossRef](#)]
32. Li, Y.; Tang, Z.; Zhang, J.; Zhang, Z. Defect engineering of air-treated WO<sub>3</sub> and its enhanced visible-light-driven photocatalytic and electrochemical performance. *J. Phys. Chem. C* **2016**, *120*, 9750–9763. [[CrossRef](#)]
33. Nakamura, I.; Negishi, N.; Kutsuna, S.; Ihara, T.; Sugihara, S.; Takeuchi, K. Role of oxygen vacancy in the plasma-treated TiO<sub>2</sub> photocatalyst with visible light activity for NO removal. *J. Mol. Catal. A Chem.* **2000**, *161*, 205–212. [[CrossRef](#)]
34. Jiang, X.; Zhang, Y.; Jiang, J.; Rong, Y.; Wang, Y.; Wu, Y.; Pan, C. Characterization of oxygen vacancy associates within hydrogenated TiO<sub>2</sub>: A positron annihilation study. *J. Phys. Chem. C* **2012**, *116*, 22619–22624. [[CrossRef](#)]
35. Xiong, T.; Cen, W.; Zhang, Y.; Dong, F. Bridging the g-C<sub>3</sub>N<sub>4</sub> interlayers for enhanced photocatalysis. *Acs Catal.* **2016**, *6*, 2462–2472. [[CrossRef](#)]
36. Wen, J.; Xie, J.; Chen, X.; Li, X. A review on g-C<sub>3</sub>N<sub>4</sub>-based photocatalysts. *Appl. Surf. Sci.* **2017**, *391*, 72–123. [[CrossRef](#)]
37. Zhao, Z.; Sun, Y.; Dong, F. Graphitic carbon nitride based nanocomposites: A review. *Nanoscale* **2015**, *7*, 15–37. [[CrossRef](#)]

38. Wu, M.; Chen, S.; Xiang, W. Oxygen vacancy induced performance enhancement of toluene catalytic oxidation using LaFeO<sub>3</sub> perovskite oxides. *Chem. Eng. J.* **2020**, *387*, 124101. [[CrossRef](#)]
39. Li, C.; Ma, D.; Mou, S.; Luo, Y.; Ma, B.; Lu, S.; Cui, G.; Li, Q.; Liu, Q.; Sun, X. Porous LaFeO<sub>3</sub> nanofiber with oxygen vacancies as an efficient electrocatalyst for N<sub>2</sub> conversion to NH<sub>3</sub> under ambient conditions. *J. Energy Chem.* **2020**, *50*, 402–408. [[CrossRef](#)]
40. Qiu, M.; Zhu, D.; Bao, X.; Wang, J.; Wang, X.; Yang, R. WO<sub>3</sub> with surface oxygen vacancies as an anode buffer layer for high performance polymer solar cells. *J. Mater. Chem. A* **2016**, *4*, 894–900. [[CrossRef](#)]
41. Qi, K.; Liu, S.-Y.; Qiu, M. Photocatalytic performance of TiO<sub>2</sub> nanocrystals with/without oxygen defects. *Chin. J. Catal.* **2018**, *39*, 867–875. [[CrossRef](#)]
42. Misra, D.; Kundu, T.K. Oxygen vacancy induced metal-insulator transition in LaNiO<sub>3</sub>. *Eur. Phys. J. B* **2016**, *89*, 4. [[CrossRef](#)]
43. Walke, P.; Gupta, S.; Li, Q.; Major, M.; Donner, W.; Mercey, B.; Lüders, U. The role of oxygen vacancies on the weak localization in LaNiO<sub>3-δ</sub> epitaxial thin films. *J. Phys. Chem. Solids* **2018**, *123*, 1–5. [[CrossRef](#)]
44. Qiao, L.; Bi, X. Direct observation of Ni<sup>3+</sup> and Ni<sup>2+</sup> in correlated LaNiO<sub>3-δ</sub> films. *EPL (Europhys. Lett.)* **2011**, *93*, 57002. [[CrossRef](#)]
45. Zheng, J.; Jiang, Q.; Lian, J. Synthesis and optical properties of flower-like ZnO nanorods by thermal evaporation method. *Appl. Surf. Sci.* **2011**, *257*, 5083–5087. [[CrossRef](#)]
46. Han, X.-G.; He, H.-Z.; Kuang, Q.; Zhou, X.; Zhang, X.-H.; Xu, T.; Xie, Z.-X.; Zheng, L.-S. Controlling morphologies and tuning the related properties of nano/microstructured ZnO crystallites. *J. Phys. Chem. C* **2009**, *113*, 584–589. [[CrossRef](#)]
47. Wang, Z.; Yang, C.; Lin, T.; Yin, H.; Chen, P.; Wan, D.; Xu, F.; Huang, F.; Lin, J.; Xie, X. Visible-light photocatalytic, solar thermal and photoelectrochemical properties of aluminium-reduced black titania. *Energy Environ. Sci.* **2013**, *6*, 3007–3014. [[CrossRef](#)]
48. Li, Y.; Yao, S.; Wen, W.; Xue, L.; Yan, Y. Sol-gel combustion synthesis and visible-light-driven photocatalytic property of perovskite LaNiO<sub>3</sub>. *J. Alloys Compd.* **2010**, *491*, 560–564. [[CrossRef](#)]
49. Clark, S.J.; Segall, M.D.; Pickard, C.J.; Hasnip, P.J.; Probert, M.I.; Refson, K.; Payne, M.C. First principles methods using CASTEP. *Z. Für Krist. -Cryst. Mater.* **2005**, *220*, 567–570. [[CrossRef](#)]
50. Perdew, J.P.; Burke, K.; Ernzerhof, M. Generalized gradient approximation made simple. *Phys. Rev. Lett.* **1996**, *77*, 3865. [[CrossRef](#)]
51. Vanderbilt, D. Soft self-consistent pseudopotentials in a generalized eigenvalue formalism. *Phys. Rev. B* **1990**, *41*, 7892. [[CrossRef](#)]
52. Monkhorst, H.J.; Pack, J.D. Special points for Brillouin-zone integrations. *Phys. Rev. B* **1976**, *13*, 5188. [[CrossRef](#)]